Origin of Pyroelectricity in Ferroelectric HfO2

J. Liu, S. Liu, L. H. Liu, B. Hanrahan, and S. T. Pantelides

Phys. Rev. Applied **12**, 034032 — Published 17 September 2019

DOI: 10.1103/PhysRevApplied.12.034032

Origin of pyroelectricity in ferroelectric HfO_2

J. Liu,[1,2*] S. Liu[3,4†], L.-H. Liu[1], B. Hanrahan[3], and S. T. Pantelides[2,5]

[1]*Optics and Thermal Radiation Research Center, Shandong University, Qingdao, Shandong 266237, China*

[2]*Department of Physics and Astronomy, Vanderbilt University, Nashville, Tennessee 37235, United States*

[3]*Sensors & Electron Devices Directorate, U.S. Army Research Laboratory, Adelphi, Maryland 20783, United States*

[4]*School of Science, Westlake University, Hangzhou, Zhejiang 310024, China*

[5]*Department of Electrical Engineering and Computer Science, Vanderbilt University, Nashville, Tennessee 37235, United States*

The pyroelectric response of materials is a promising phenomenon that is used in many applications. Here we report first-principles lattice dynamics and *ab-initio* molecular dynamics calculations to investigate the mechanisms of the pyroelectric effect in the $Pca2_1$ orthorhombic phase of HfO_2, an emerging pyroelectric material with promising technological applications. With first-principles lattice dynamics calculations, we demonstrate a large pyroelectric response that is intrinsic to the *pure* $Pca2_1$ orthorhombic phase. Unlike most conventional ferroelectric pyroelectrics, such large pyroelectricity arises unexpectedly from the secondary effect (induced by the negative longitudinal piezoelectric effect) that has not received due attention. *Ab-initio* molecular dynamics simulations further demonstrate a giant pyroelectric response that is associated with an orthorhombic(polar)-to-tetragonal(nonpolar) structural phase transition. Upon the incorporation of Si dopants with increasing dopant concentrations, the phase transition persists but occurs at reduced temperatures with enhanced pyroelectric responses. The present work unravels and highlights the secondary pyroelectric effect that is responsible for the pyroelectricity in HfO_2, and discusses its promising potential for applications.

---

*Jian.Y.Liu@sdu.edu.cn, †liushi@westlake.edu.cn.

I. INTRODUCTION

All ferroelectrics carry a spontaneous polarization that varies with temperature[1,2]. The change in polarization resulting from a temperature variation generates a voltage, which is known as pyroelectricity[1,2]. Thus, all ferroelectrics are pyroelectric, but the inverse is not necessarily true. The pyroelectric response is the key property that is responsible for a wide range of applications such as thermal imaging[2,3] and pyroelectric energy harvesting[4,5]. Despite the fundamental interest and the concomitant technological importance, first-principles investigations of the pyroelectric effect have not received due attention. As a result, a satisfactory understanding of the pyroelectric effect is still lacking, especially for new pyroelectric/ferroelectric materials. For example, an unusually large secondary pyroelectricity (associated with piezoelectricity and thermal expansion) has recently been demonstrated for group-IV monochalcogenide monolayers[6-9], contrary to the general belief for bulk prototypical ferroelectric pyroelectrics that the secondary effect plays a minor role[2].

The recent discovery of unexpected ferroelectricity (and hence pyroelectricity) in both *pure* and doped hafnia (HfO_2) thin films[10,11] combined with their great CMOS (complementary metal oxide semiconductor) compatibility make hafnia a promising candidate for nanoscale device applications such as pyroelectric energy harvesting and infrared detection[12-14]. While it has been theoretically demonstrated that Si doping promotes the stabilization of the orthorhombic phase of HfO_2[15,16], doping[12,17] and alloying[18] are promising methods for tuning the pyroelectric response of HfO_2-based pyroelectrics. Large pyroelectric response has been observed in Si-doped HfO_2 thin films, attributed to the temperature- and field-induced orthorhombic(polar)-to-tetragonal(nonpolar) transition[12]. Very recently, scattered data of pyroelectric coefficients that vary with dopant concentration, film thickness, and wake-up cycles have been reported for Si-doped

HfO_2[12,17,19-21]. Further development and optimization of HfO_2-based pyroelectric devices require a detailed quantitative understanding of the nature of the pyroelectricity in ferroelectric HfO_2. Reliable interatomic potentials are still lacking for HfO_2, preventing large-scale finite-temperature MD simulations.

In the first part of this paper, we use the recently developed first-principles lattice-dynamics approach to identify the underlying mechanisms responsible for the promising pyroelectric effect in *pure* ferroelectric HfO_2, at temperatures below the ferroelectric-to-paraelectric transition temperature. Unlike in most conventional ferroelectric pyroelectrics, we demonstrate a large and dominating secondary pyroelectric response in the $Pca2_1$ orthorhombic phase of *pure* HfO_2, induced by a significant negative longitudinal piezoelectricity together with an isotropic positive thermal expansion. In the second part of this paper, we perform *ab-initio* molecular dynamics simulations to further demonstrate that the secondary effect is associated with an orthorhombic(polar)-to-tetragonal(nonpolar) structural phase transition at around 850 K. The transition "pathway" involves translational displacements of Hf and O sublattices towards their centrosymmetric positions, and no order-disorder character is identified. Furthermore, the phase transition persists with the incorporation of Si dopants. With increasing dopant concentrations, the transition temperature is reduced and the primary pyroelectric response is enhanced, because substitutional Si doping perturbs the local chemical environment, introducing strong anharmonicity to the host HfO_2 structure. The present work unravels and highlights the secondary pyroelectric effect that is responsible for the pyroelectricity in HfO_2, and discusses its important implications for practical energy and sensor applications utilizing HfO_2-based pyroelectrics.

II. THEORY

At temperatures below the ferroelectric-to-paraelectric phase transition temperature, pyroelectricity[22] (defined as the response of the spontaneous polarization P_s with respect to fluctuations in temperature T) at constant stress σ is conventionally separated into two parts[2,23,24]: the primary (at constant external strain ε) $\Pi_1(T)$ and the secondary $\Pi_2(T)$:

$$\Pi = \left(\frac{dP_S}{dT}\right)_\sigma = \left(\frac{\partial P_S}{\partial T}\right)_\varepsilon + \sum_i \left(\frac{\partial P_S}{\partial \varepsilon_i}\right)_T \left(\frac{\partial \varepsilon_i}{\partial T}\right)_\sigma. \quad (1)$$

The secondary part $\Pi_2(T)$ accounts for the pyroelectricity that is associated with piezoelectricity and thermal expansion. It can be readily obtained from the piezoelectric stress constants e ($\partial P_S/\partial \varepsilon_i$) and the thermal expansion coefficients α ($\partial \varepsilon_i/\partial T$), and is generally much smaller than the primary part for conventional ferroelectrics[2]. The primary part $\Pi_1(T)$, on the other hand, accounts for the "clamped-lattice" pyroelectricity. With the fixed lattice parameters, the internal structural parameters vary with temperature (referred to as "internal" thermal expansion in this paper, by analogy with "thermal expansion" that describes the variation of lattice parameters with temperature). The change of P_S with respect to atomic displacements, ($\partial P_S/\partial Q_{\vec{0}j}$), defines Born effective charges (BEC) Z^*[25]. It is then clear that part of primary pyroelectricity arises as the lattice exhibits "internal thermal expansion" while ions carry rigid BECs. This picture is usually referred to as the point-charge or rigid-ion model[26,27], as the renormalization of BECs due to electron-phonon interactions is neglected. The corresponding rigid-ion primary pyroelectricity reads[6,28]

$$\left(\frac{\partial P_S}{\partial T}\right)_\varepsilon = \sum_j \left(\frac{\partial P_S}{\partial Q_{\vec{0}j}}\right)_T \left(\frac{\partial \langle Q_{\vec{0}j}\rangle}{\partial T}\right)_\varepsilon, \quad (2)$$

where the Q's are the normal-mode amplitudes, and the summation j runs over $\vec{q} = 0$ optical modes of symmetries allowing non-vanishing contributions ($\langle Q_{\vec{0}j}\rangle \neq 0$). $\langle Q_{\vec{0}j}\rangle$ is calculated with the quasi-harmonic approximation[6,28],

$$\langle Q_{\vec{0}j}\rangle = -\sum_{\vec{q}\lambda} \frac{\hbar}{2} \frac{2n_{\vec{q}\lambda}+1}{\omega^2_{\vec{0}j}} \frac{\partial \omega_{\vec{q}\lambda}}{\partial Q_{\vec{0}j}}, \quad (3)$$

where ω are the phonon eigenfrequencies of mode λ at wavevector $\vec{q}$, and n is the Bose-Einstein distribution function.

III. METHODS

Density-functional theory (DFT) total-energy and density-functional perturbation theory (DFPT) lattice dynamics calculations[29] have been performed using the QUANTUM ESPRESSO package[30]. Spontaneous polarization is calculated using the modern theory of polarization (Berry-phase method)[25,31-33]. For the electronic-structure calculations, we use the

LDA functional[34] for HfO_2. Ultrasoft pseudopotentials are taken from the PSLibrary[35]. The electronic wave-functions are expanded in a plane-wave basis with a kinetic energy cuto□ of 140 Ry. For Brillouin-zone sampling, 4×4×4 k-point mesh is used. Phonons are calculated on the same q-point mesh. All the structure figures are produced using VESTA[36]. In Eq. (3), to compute $\partial\omega_{\vec{q}\lambda}/\partial Q_{\vec{0}j}$, a central difference scheme is used through displacing atoms in the unit cell collectively by $Q_{\vec{0}j}$. Details of the first-principles lattice dynamics method can be found in Ref. [28].

Ab initio molecular dynamics (AIMD) simulations are performed using a basis of linear combinations of localized atomic orbitals, as implemented in the SIESTA package[37]. The $Pca2_1$ orthorhombic phase of HfO_2 is modelled by a supercell of 324 atoms (3×3×3 unit cells). To model Si-doped HfO_2, 2 and 4 Hf atoms are replaced by Si atoms, corresponding to substitutional doping concentration of 1.85 and 3.7 cat% respectively. A variationally optimized double-ζ polarized basis set is used with a mesh cutoff of 250 Ry for the real-space grid. Temperature is raised sequentially, i.e. the initial position and velocity of the simulation at a higher temperature are generated from the final snapshot of the simulation at a lower temperature. For each AIMD simulation, a trajectory of 0.5 ps is used for production after an equilibration stage of 0.5 ps, with a time step of 1 fs. To highlight the secondary pyroelectric effect, simulations are performed within the *NVT* and *NPT* ensembles, with temperature and pressure controlled by a Nosé thermostat[38] and Parrinello-Rahman barostat[39] respectively. Spontaneous polarization is evaluated for the ensemble-averaged structure at each temperature.

The pyroelectric coefficient was determined for a 5 at% Al-doped HfO_2 thin film, in a manner similar to Refs. [40,41]. The film was grown on 100 nm-thick, reactively sputtered TiN on a silicon substrate. The ALD process used metal organic precursors tetrakis (ethylmethylamino) hafnium (TEMAH) and trimethylaluminium (TMA) for the cations and ozone was used as the oxidant with argon as a carrier gas. The Al_2O_3 content was defined by using a 1:19 cycle ratio. The total film thickness of 20 nm was achieved by altering the number of supercycles, monitored *in situ* via ellipsometry. A TiN top electrode was reactively sputtered then defined using the RCA-1 etch. Samples were annealed at 700 °C for 20 s in an N_2 environment. The pyroelectric coefficient was determined by oscillating the temperature of a TiN/Al-HfO_2/TiN capacitor and measuring the generated current. To determine the sample temperature, a calibrated resistive thermal device chip was co-located on a hotplate with the Al-HfO_2 capacitor. The temperature and current profiles were used to determine the pyroelectric coefficient Π

$$I_p = \Pi A \frac{dT}{dt}, \tag{4}$$

where I_p is the pyroelectric current, A is the capacitor area, and $\frac{dT}{dt}$ is the temperature rate of change. See detailed experimental setups in Refs. [40,41].

IV. RESULTS

Hafnia HfO_2 in the bulk state is nonpolar as its room-temperature monoclinic $P2_1/c$ phase is centrosymmetric[42]. A consensus has seemingly been reached that the origin of the unexpected ferroelectricity in HfO_2 thin film is due to the $Pca2_1$ orthorhombic phase probably stabilized by a variety of extrinsic factors such as residual stresses, dopants, oxygen vacancies, and the surface effect in small grains[10,11,43-47]. Ferroelectricity has also been observed in undoped HfO_2 thin film[48]. It was found that the polar $Pca2_1$ orthorhombic phase and the associated nonpolar $P4_2/nmc$ tetragonal phase are both dynamically stable, while the latter corresponds to a very shallow minimum of the energy landscape[42]. Our calculated lattice parameters for *a*, *b*, and *c* are 5.13, 4.92, and 4.95 Å respectively, while the computed spontaneous polarization is 56 μC/cm^2 (taking the $P4_2/nmc$ tetragonal phase as the reference), in line with previous theoretical results based on a different exchange-correlation functional[42].

We first apply the lattice-dynamics approach to study the pyroelectricity in the *pure* $Pca2_1$ orthorhombic phase of HfO_2 (referred to as *pure* HfO_2 hereafter). The calculated room-temperature "intrinsic" (dopant-free and strain-free) Π reads -38 μC/(m^2·K), smaller in magnitude than the maximum values of Π reported for Si-doped HfO_2[17,19,20] (Π varies with dopant concentration and film thickness), while our measurement for Al-doped HfO_2 thin film reads -36 μC/(m^2·K), as shown in Fig. 1a. These results demonstrate that the pyroelectric effect observed in Si-doped HfO_2 can be largely accounted for by its "intrinsic" pyroelectricity. We will discuss the effects of Si doping shortly. In most conventional ferroelectric pyroelectrics,

the primary pyroelectricity dominates the pyroelectric effect[2]. Surprisingly, in *pure* HfO_2, the secondary pyroelectricity dominates, as shown in Fig. 1a.

Understanding the underlying mechanism responsible for such intriguing pyroelectric response is of great importance for further improvement of future pyroelectric applications. In conventional ferroelectrics such as $PbTiO_3$[49] and non-ferroelectrics such as wurtzite semiconductors[25], the piezoelectric coefficients along the polar axis (e_{33}) and in the basal plane (e_{31}) are positive and negative respectively, i.e. these materials exhibit "normal" piezoelectricity. One often-mentioned exception is the case of ferroelectric polymer poly(vinylidene fluoride) (PVDF) in which e_{33} is negative[50]. More recently, such unusual negative longitudinal piezoelectric effect was also found in several hexagonal *ABC* ferroelectrics[51]. We found significant negative longitudinal piezoelectricity in *pure* HfO_2, as shown in Fig. 1b. Considering the isotropic positive thermal expansion (see the inset of Fig. 1b), this results in significant secondary pyroelectric effect ($\Pi_2=\sum_j e_{cj}\alpha_j$, c being the polar axis). Note that significant secondary pyroelectricity could also arise in a different way, e.g. in the cases of $PbTiO_3$ and group-IV monochalcogenide monolayers[7] which show "normal" piezoelectricity but anisotropic thermal expansion (the two lattice constants along and perpendicular to the polar axis become shorter and longer with increasing temperatures respectively).

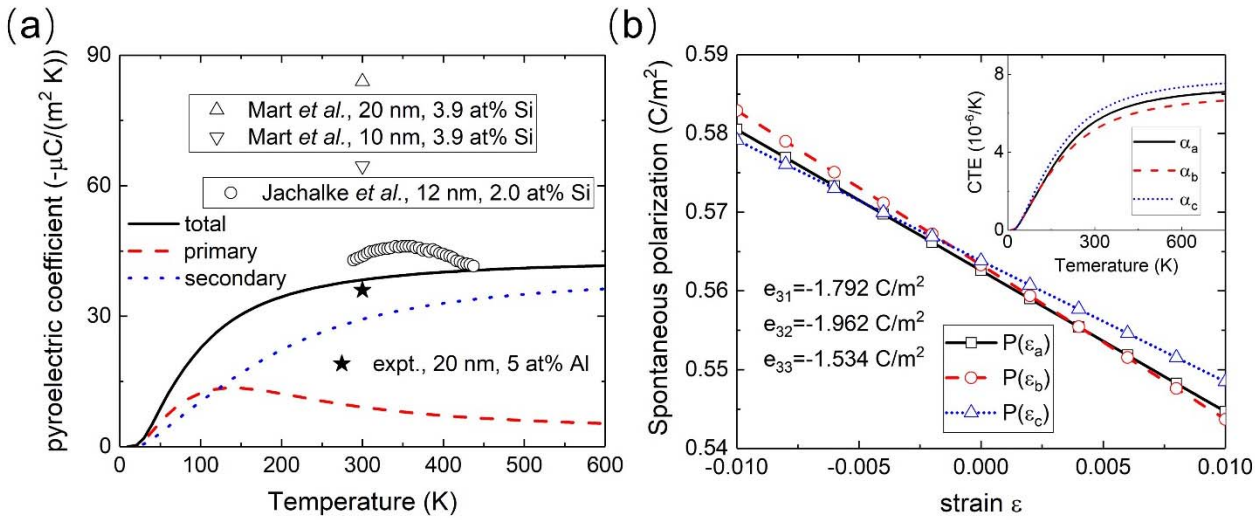

Figure 1. For the *pure* $Pca2_1$ orthorhombic phase of HfO_2: (a) Calculated primary and secondary pyroelectric coefficients, compared with experimental data for Al-doped (this work) and Si-doped (maximum values in each experiment) HfO_2 thin film. (b) Calculated piezoelectric (main panel) and thermal expansion (inset) components in the secondary pyroelectric effect. Note that e_{33} is negative, i.e. *pure* HfO_2 exhibits negative longitudinal piezoelectricity.

The primary pyroelectricity, on the other hand, is intimately related to the anharmonicity of the lattice. In line with the fact that the paraelectric $P4_2/nmc$ tetragonal phase is dynamically stable (not a saddle point in potential energy surface), the absence of a polar soft phonon mode is indicative of insignificant rigid-ion primary pyroelectricity. The eight zone-center phonon modes with A_1-TO symmetry that are responsible for the rigid-ion primary pyroelectricity (due to their non-vanishing mean normal mode amplitudes $\langle Q_{\bar{0}j}\rangle$) are shown in Fig. 2. These phonon modes are only slightly anharmonic, as manifested in the almost parabolic shape of the energy landscape (calculated with ions statically displaced over a range of "frozen-in" normal-mode amplitudes). As a result, their contributions to $\Pi_1(T)$ are relatively insignificant (see Fig. S1 in Supplemental Material [52]).

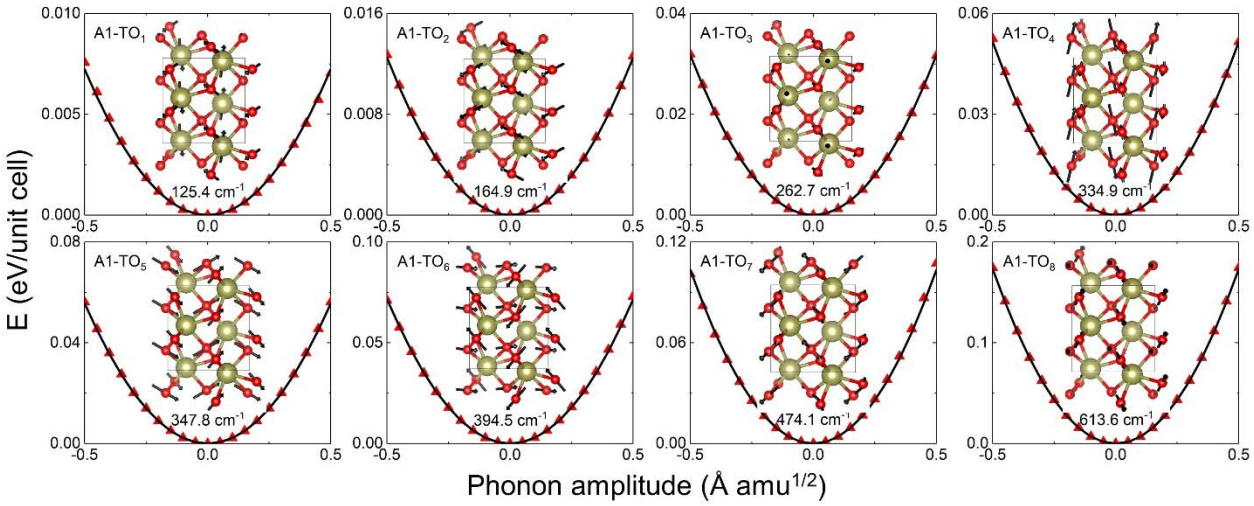

Figure 2. Zone-center TO phonon modes with A_1 symmetry. The arrows attached on the ions (Hf in brass, and O in red) indicate the eigenvector. Energies (triangles) are calculated with ions statically displaced over a range of "frozen-in" normal-mode amplitudes. The fitted harmonic potentials are shown by curves, while the legends indicate the corresponding eigenfrequencies.

We have demonstrated that the large pyroelectric response (comparable to that of many commercially used pyroelectrics) is an intrinsic property of *pure* HfO_2, and arises unexpectedly from the secondary pyroelectric effect. To further demonstrate the secondary pyroelectric effect, we performed AIMD simulations within the *NVT* and *NPT* ensembles, where thermal expansion is forbidden and allowed respectively. The comparison is shown in the top panel of Fig. 3a. In the *NVT* simulations, only the primary pyroelectric effect is included. An insignificant primary pyroelectricity is observed, as reflected by the temperature-independent spontaneous polarization, consistent with our lattice-dynamics calculations. The small discrepancy is possibly due to the rather weak anharmonic nature of the corresponding phonon modes, and the limited time- and length-scales achievable by AIMD simulations. In the *NPT* simulations, the secondary pyroelectric effect is included as well. A large pyroelectric response is found, highlighted by the largely "isotropic" thermal expansion (the values of *a*, *b*, and *c* all increase with increasing temperature).

More importantly, the secondary pyroelectric response is associated with a structural phase transition, after which the two lattice parameters *b* and *c* become equal, as shown in the bottom panel of Fig. 3a. Such orthorhombic(polar)-to-tetragonal(nonpolar) transition (see Fig. 3b, and Supplemental Material for an AIMD movie at the transition) is in agreement with the experimental observations for Si-doped HfO_2 thin film[12,17]. The calculated transition temperature T_c for *pure* HfO_2 is around 850 K (750 K using the Perdew-Burke-Ernzerhof (PBE) functional[53], as shown in Fig. S2, demonstrating that the phase transition behavior is not substantially sensitive to the choice of density functional). It is noted that the exact value of T_c may be dependent on the size of the supercell. However, an accurate determination of T_c is beyond the scope of this work. The calculated T_c is higher than those reported for Si-doped HfO_2 which vary with dopant concentration and film thickness[12,17], suggesting that the orthorhombic-to-tetragonal transition is an intrinsic property of *pure* HfO_2, i.e. the phase transition is not necessarily induced by the incorporation of Si dopants. The peak pyroelectric response near the transition is estimated roughly to be as large as -2400 μC/(m^2·K), comparable to the pyroelectric response of up to -1300 μC/(m^2·K) (Si-doped HfO_2, 9 nm, 5.6 at%) reported by Hoffmann *et al.*[12].

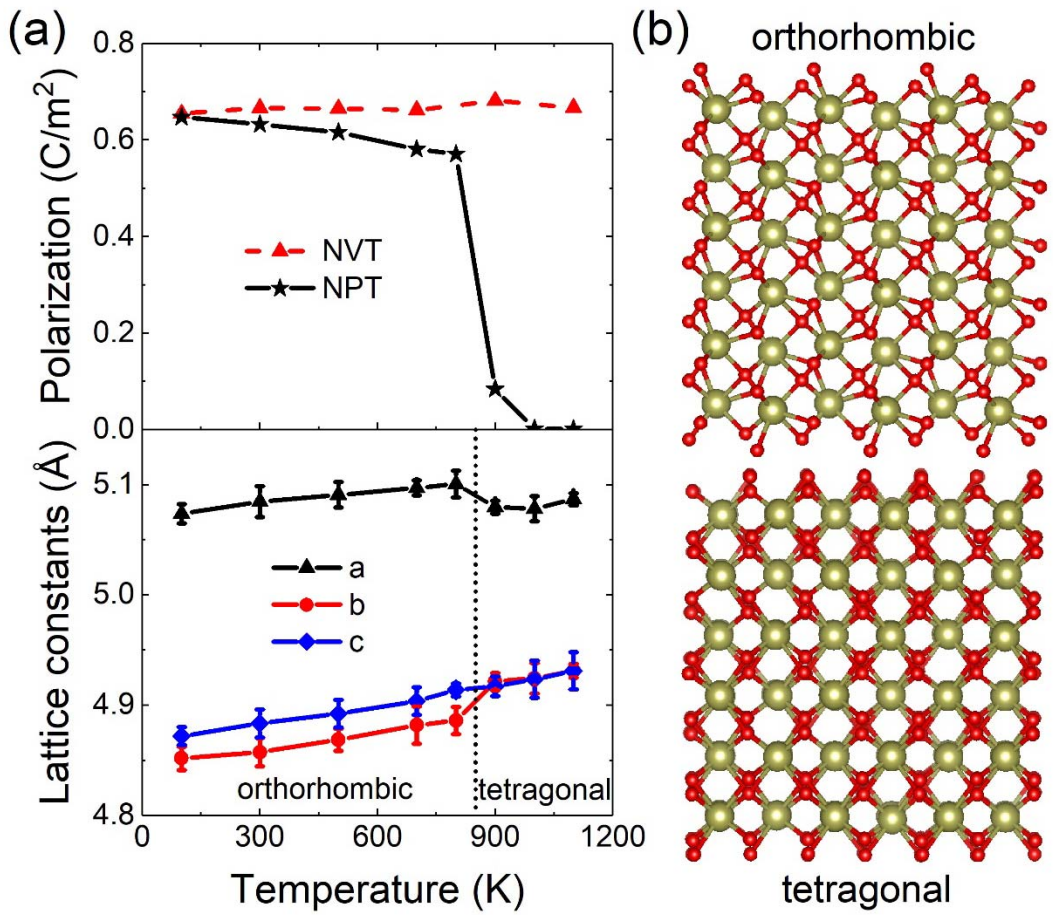

Figure 3. (a) Top panel: pyroelectric response calculated with AIMD simulations. Bottom panel: temperature-dependent lattice constants calculated in the *NPT* simulations. The orthorhombic-to-tetragonal transition occurs at around 850 K, before and after which the two phases exhibit normal thermal expansion behaviors. (b) Mean (ensemble-averaged) structures of the orthorhombic and tetragonal phases evaluated at 300 and 1100 K respectively.

The orthorhombic-to-tetragonal transition is found to exhibit a notable displacive character, as shown in Fig. 4a. To demonstrate this, we define a parameter δ as the relative distance (in fraction of lattice constant *c*) between the O- and Hf-planes in the polar direction (see the inset of Fig. 4a). The probability distribution of δ exhibits a single peak at each temperature. With increasing temperatures, the peak broadens and shifts to the value of 0.25 that corresponds to the centrosymmetric positions along the polar direction. In our AIMD simulations, the transition occurs at around 850 K. To highlight the transition "pathway", the instantaneous unit-cell structures (projected from the supercell structures) during the transition are shown in Fig. 4b. The transition "pathway" involves translational displacements of Hf and O sublattices towards their centrosymmetric positions (see the arrows in the upper-left panel of Fig. 4b, and the animated movie of the orthorhombic-to-tetragonal transition in Supplemental Material). This displacement pattern is possibly indicative of a soft-mode-like behavior near the transition that is otherwise absent in the (zero-temperature) metastable tetragonal phase of HfO_2. Note that, within the time- and length-scales achieved by AIMD simulations, we are unable to identify any order-disorder character in the orthorhombic-to-tetragonal transition.

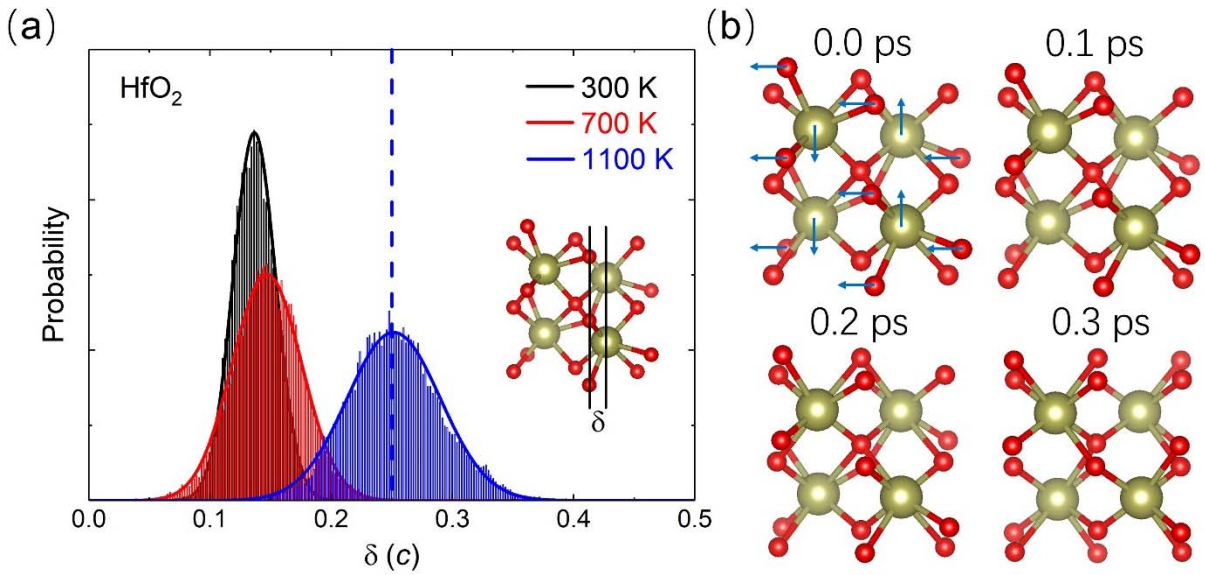

Figure 4. (a) Probability distribution of the atomic displacement for *NPT* simulations at selected temperatures. The atomic displacement δ is the relative distance between the O- and Hf-planes in the polar direction, defined in fraction of the lattice constant *c* (δ=0.25 corresponds to the tetragonal phase). (b) The instantaneous unit-cell structures (projected from supercell structures) at selected time frames during the phase transition for the *NPT* simulation at 900 K.

Last but not least, we investigate the effects of Si doping on the pyroelectric response of orthorhombic HfO_2, for which seemingly contradictory experimental results were reported very recently[12,17,19]. Upon the incorporation of Si dopants with increasing dopant concentrations, we find that the aforementioned orthorhombic-to-tetragonal transition persists but occurs at reduced temperatures, as shown in Fig. 5a. As a result, the pyroelectric coefficients increase in magnitude with increasing dopant concentrations. This tendency is in remarkable agreement with the experimental observations found for Si-doped HfO_2 thin film[12,17]. For example, Hoffmann *et al.*[12] obtained pyroelectric coefficients of -950, -1100, and -1300 μC/(m^2·K) for 3.8, 4.3, and 5.6 at% Si-doped HfO_2, while the phase transition temperatures (at which the remanent polarization is reduced by half) are estimated to be 410, 330, and 170 K respectively. Also, it could be expected that the pyroelectric behavior eventually vanishes with further increasing the Si dopant concentrations, as observed in experiments[17,19].

Unlike the case of *pure* HfO_2, we find that the enhanced pyroelectric response for Si-doped HfO_2 arises mainly from the primary pyroelectric effect. Note that the two key components that determine the primary pyroelectricity are the atomic displacements of ions and the BECs they carry. While Si and Hf ions are equivalent (in the sense that they carry similar BECs), their local coordination environments are fundamentally different[16]. Hence, the incorporation of Si dopants perturbs the host HfO_2 structure and introduces strong anharmonicity (in particular along the polar direction, see Fig. S3), resulting in notable atomic displacements (and hence primary pyroelectricity), as shown in Fig. 5b. We further corroborate this conclusion by noting that piezoelectricity and thermal expansion of the lattice, i.e. the two key components that determine the secondary pyroelectricity, do not vary with Si dopant concentrations, as shown in Fig. S4. Note also that the negative longitudinal piezoelectric effect found in *pure* HfO_2 persists in Si-doped HfO_2.

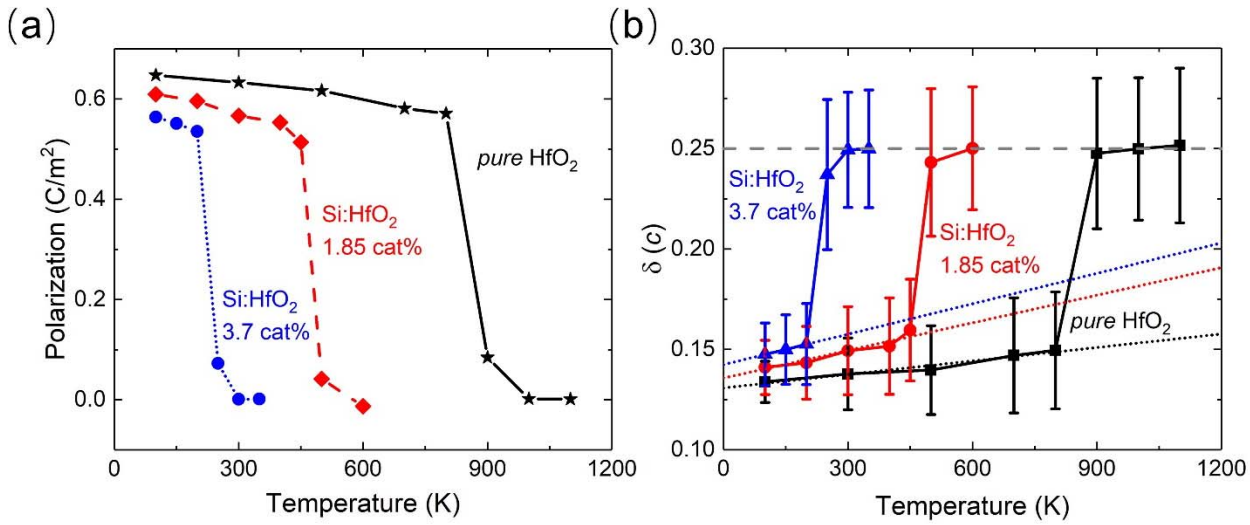

Figure 5. For the *pure* and Si-doped HfO_2: (a) Pyroelectric response calculated with AIMD simulations. Si-doped HfO_2 is modelled by substitute 2 (1.85 cat%) and 4 (3.7 cat%) Hf atoms with Si atoms in a supercell of 324 atoms. (b) Temperature-dependent atomic displacement δ (see Fig. 4a for definition). The dotted lines represent the notable atomic displacement introduced by the incorporation of Si dopants.

V. DISCUSSION

The pyroelectric response determines the performance of a material in various device applications such as thermal infrared sensors and pyroelectric energy harvesters. The above theoretical investigations have demonstrated large *intrinsic* (the material is free to expand thermally) secondary pyroelectricity in HfO_2. This feature suggests that straining the lattice might have a significant impact on the performance of HfO_2-based pyroelectrics. Indeed, in pyroelectric measurements, the pyroelectric thin film rigidly attached to a thick substrate is free to expand only in the thickness dimension[54]. The thermal expansion mismatch between the film (α_1^{film}) and the substrate (α_1^{sub}) causes an *extrinsic* (in the basal plane the thermal expansion of the film is subject to that of the substrate) pyroelectric effect via the piezoelectricity of the film (d_{31}). To determine such impact, a wide-frequency-range method has been demonstrated in pyroelectric measurements[55,56]. In the literature[55,56], at low frequencies the film expands in plane with the substrate, while at high frequencies the film is clamped to the substrate at constant temperature. The effective low-frequency (Eq. 9 in Ref. [54]) and high-frequency (Eq. 8 in Ref. [54]) pyroelectric coefficients read[55] (s is the elastic compliance constant)

$$\Pi^{\text{low}} = \Pi - \frac{2d_{31}\left(\alpha_1^{\text{film}} - \alpha_1^{\text{sub}}\right)}{s_{11}+s_{12}}. \tag{5a}$$

$$\Pi^{\text{high}} = \Pi - \frac{2d_{31}\alpha_1^{\text{film}}}{s_{11}+s_{12}}. \tag{5b}$$

The difference, $2d_{31}\alpha_1^{\text{sub}}/(s_{11}+s_{12})$, yields the coupling between the piezoelectricity of the film and the in-plane thermal expansion of the substrate[55]. This term, also referred to as the "secondary" pyroelectricity in some pyroelectric measurements[55-57], needs to be distinguished from the *intrinsic* Π_2.

Last but not least, for the purpose of characterizing/enhancing the pyroelectric response utilizing HfO_2-based pyroelectrics in applications, some important implications can be made. Mart *et al.*[57] used the wide-frequency-range method to characterize the pyroelectric response of Si-doped HfO_2, and obtained the "secondary" pyroelectric coefficient ($\Pi^{\text{low}} - \Pi^{\text{high}}$) of -19 μC/(m^2·K), comparable to the calculated *intrinsic* Π_2 of -29 μC/(m^2·K) for *pure* HfO_2. This highlights the "secondary" contribution from the in-plane thermal expansion of the substrate. Noting that d_{31} is typically negative, a direct comparison of the thermal expansion coefficients of the film (calculated, $\alpha_1^{\text{film}} \approx 5.6\times10^{-6}$/K) and the substrate (e.g., using TiN as top and bottom electrodes[17,19,20,57], measured[58], $\alpha_1^{\text{sub}} \approx 9.9\times10^{-6}$/K) indicates that Π^{low} and Π^{high} are negative (overestimating Π) and positive (underestimating Π) respectively. This partly explains the fact that our theoretical Π for *pure* HfO_2 is smaller in magnitude than low-frequency measurements for Si-doped HfO_2[19,20,57]. In low-frequency pyroelectric

applications, the pyroelectric response can be further enhanced by depositing HfO_2 thin film on substrates with much larger coefficient of thermal expansion[40].

As for Si-doped HfO_2, Π (mainly Π_1) becomes larger in magnitude with increasing doping concentration as a result of reduced transition temperature, suggesting that Si doping not only promotes the stabilization but also enhances the primary pyroelectric response. We have attributed the enhanced primary pyroelectricity to the perturbation of local chemical environment due to Si doping. Considering that Si and Hf ions are equivalent, one can expect that the incorporation of other dopants (e.g., divalent dopants such as Sr, trivalent dopants such as Y, and four-valent dopants such as Ce) may further enhance the pyroelectric response. In fact, these dopants have been revealed as promising candidates to promote ferroelectricity in HfO_2[15,16]. The effect of these dopants on pyroelectricity will be discussed in a future work.

V. CONCLUSIONS

In summary, we have applied a first-principles lattice-dynamics approach to identify the underlying mechanisms responsible for pyroelectricity in the recently discovered ferroelectric phase of HfO_2. Unlike most conventional ferroelectric pyroelectrics, the secondary pyroelectricity dominates in the $Pca2_1$ orthorhombic phase of *pure* HfO_2, due to an unusual negative longitudinal piezoelectricity together with an isotropic positive thermal expansion. We further demonstrate with AIMD simulations that the secondary effect is associated with an orthorhombic(polar)-to-tetragonal(nonpolar) structural phase transition. The phase transition occurs at around 850 K and is identified to be displacive. With the incorporation of Si dopants, such phase transition persists but occurs at reduced temperatures. Si-doping perturbs the host HfO_2 structure, introducing strong anharmonicity and hence the primary pyroelectric response is enhanced. The present work unravels and highlights the secondary pyroelectric effect that is responsible for the pyroelectricity in HfO_2 and provides important implications for practical applications utilizing HfO_2-based pyroelectrics. In pursuit of enhanced pyroelectric response, substrates that exhibit large thermal expansion and dopants that strongly perturb the host HfO_2 structure are desired.

This work was supported by the McMinn Endowment at Vanderbilt University. J. L. was supported by the Qilu Young Scholar Program of Shandong University. Computations were carried out at the National Energy Research Scientific Computing Center, a DOE Office of Science User Facility supported by the Office of Science of the U.S. Department of Energy under Contract No. DE-AC02-05CH11231. This work used the Extreme Science and Engineering Discovery Environment (XSEDE), which is supported by National Science Foundation grant number ACI-1548562, through allocation TG-DMR170102. J. L. acknowledge the Texas Advanced Computing Center (TACC) at The University of Texas at Austin for providing HPC resources that have contributed to the research results reported in this paper. S. L. is supported by SEDD Distinguished Postdoc Fellowship at US Army Research Laboratory.

[1] Damjanovic D., Ferroelectric, dielectric and piezoelectric properties of ferroelectric thin films and ceramics, *Rep. Prog. Phys.* **61**, 1267 (1998).

[2] Lang S. B., Pyroelectricity: from ancient curiosity to modern imaging tool, *Phys. Today* **58**, 31 (2005).

[3] Whatmore R. W., Pyroelectric devices and materials, *Rep. Prog. Phys.* **49**, 1335 (1986).

[4] Yang Y., Wang S., Zhang Y. and Wang Z. L., Pyroelectric nanogenerators for driving wireless sensors, *Nano Lett.* **12**, 6408 (2012).

[5] Yang Y., Guo W., Pradel K. C., Zhu G., Zhou Y., Zhang Y., Hu Y., Lin L. and Wang Z. L., Pyroelectric nanogenerators for harvesting thermoelectric energy, *Nano Lett.* **12**, 2833 (2012).

[6] Liu J. and Pantelides S. T., Mechanisms of pyroelectricity in three-and two-dimensional materials, *Phys. Rev. Lett.* **120**, 207602 (2018).

[7] Liu J. and Pantelides S. T., Anisotropic thermal expansion of group-IV monochalcogenide monolayers, *Appl. Phys. Express* **11**, 101301 (2018).

[8] Mehboudi M., Fregoso B. M., Yang Y., Zhu W., van der Zande A., Ferrer J., Bellaiche L., Kumar P. and Barraza-Lopez S., Structural phase transition and material properties of few-layer monochalcogenides, *Phys. Rev. Lett.* **117**, 246802 (2016).
[9] Barraza-Lopez S., Kaloni T. P., Poudel S. P. and Kumar P., Tuning the ferroelectric-to-paraelectric transition temperature and dipole orientation of group-IV monochalcogenide monolayers, *Phys. Rev. B* **97**, 024110 (2018).
[10] Böscke T., Müller J., Bräuhaus D., Schröder U. and Böttger U., Ferroelectricity in hafnium oxide thin films, *Appl. Phys. Lett.* **99**, 102903 (2011).
[11] Müller J., Böscke T. S., Schröder U., Mueller S., Bräuhaus D., Böttger U., Frey L. and Mikolajick T., Ferroelectricity in simple binary ZrO_2 and HfO_2, *Nano Lett.* **12**, 4318 (2012).
[12] Hoffmann M., Schroeder U., Künneth C., Kersch A., Starschich S., Böttger U. and Mikolajick T., Ferroelectric phase transitions in nanoscale HfO_2 films enable giant pyroelectric energy conversion and highly efficient supercapacitors, *Nano Energy* **18**, 154 (2015).
[13] Park M. H., Lee Y. H., Kim H. J., Kim Y. J., Moon T., Kim K. D., Mueller J., Kersch A., Schroeder U. and Mikolajick T., Ferroelectricity and Antiferroelectricity of Doped Thin HfO_2 ‐ Based Films, *Adv. Mater.* **27**, 1811 (2015).
[14] Park M. H., Kim H. J., Kim Y. J., Moon T., Do Kim K. and Hwang C. S., Toward a multifunctional monolithic device based on pyroelectricity and the electrocaloric effect of thin antiferroelectric $Hf_xZr_{1-x}O_2$ films, *Nano Energy* **12**, 131 (2015).
[15] Batra R., Huan T. D., Rossetti Jr G. A. and Ramprasad R., Dopants promoting ferroelectricity in Hafnia: Insights from A comprehensive chemical space exploration, *Chem. Mater.* **29**, 9102 (2017).
[16] Künneth C., Materlik R., Falkowski M. and Kersch A., Impact of four-valent doping on the crystallographic phase formation for ferroelectric HfO_2 from first-principles: Implications for ferroelectric memory and energy-related applications, *ACS Appl. Nano Mater.* **1**, 254 (2018).
[17] Park M. H., Chung C. C., Schenk T., Richter C., Hoffmann M., Wirth S., Jones J. L., Mikolajick T. and Schroeder U., Origin of Temperature ‐ Dependent Ferroelectricity in Si ‐ Doped HfO_2, *Adv. Electron. Mater.* **4**, 1700489 (2018).
[18] Smith S., Kitahara A., Rodriguez M., Henry M., Brumbach M. and Ihlefeld J., Pyroelectric response in crystalline hafnium zirconium oxide ($Hf_{1-x}Zr_xO_2$) thin films, *Appl. Phys. Lett.* **110**, 072901 (2017).
[19] Jachalke S., Schenk T., Park M. H., Schroeder U., Mikolajick T., Stöcker H., Mehner E. and Meyer D. C., Pyroelectricity of silicon-doped hafnium oxide thin films, *Appl. Phys. Lett.* **112**, 142901 (2018).
[20] Mart C., Kämpfe T., Zybell S. and Weinreich W., Layer thickness scaling and wake-up effect of pyroelectric response in Si-doped HfO_2, *Appl. Phys. Lett.* **112**, 052905 (2018).
[21] Pandya S., Velarde G., Zhang L. and Martin L. W., Pyroelectric and electrocaloric effects in ferroelectric silicon-doped hafnium oxide thin films, *Phys. Rev. Mater.* **2**, 124405 (2018).
[22] Resta R., Electrical polarization and orbital magnetization: the modern theories, *J. Phys. Condens. Matter* **22**, 123201 (2010).
[23] Szigeti B., Temperature dependence of pyroelectricity, *Phys. Rev. Lett.* **35**, 1532 (1975).
[24] Born M., On the quantum theory of pyroelectricity, *Rev. Mod. Phys.* **17**, 245 (1945).
[25] Bernardini F., Fiorentini V. and Vanderbilt D., Spontaneous polarization and piezoelectric constants of III-V nitrides, *Phys. Rev. B* **56**, R10024 (1997).
[26] Belabbes A., Furthmüller J. and Bechstedt F., Relation between spontaneous polarization and crystal field from first principles, *Phys. Rev. B* **87**, 035305 (2013).
[27] Peng Q. and Cohen R. E., Origin of pyroelectricity in $LiNbO_3$, *Phys. Rev. B* **83**, 220103 (2011).

[28] Liu J., Fernández-Serra M. V. and Allen P. B., First-principles study of pyroelectricity in GaN and ZnO, *Phys. Rev. B* **93**, 081205 (2016).
[29] Mounet N. and Marzari N., First-principles determination of the structural, vibrational and thermodynamic properties of diamond, graphite, and derivatives, *Phys. Rev. B* **71**, 205214 (2005).
[30] Giannozzi P. *et al.*, QUANTUM ESPRESSO: a modular and open-source software project for quantum simulations of materials, *J. Phys.: Condens. Matter* **21**, 395502 (2009).
[31] King-Smith R. and Vanderbilt D., Theory of polarization of crystalline solids, *Phys. Rev. B* **47**, 1651 (1993).
[32] Resta R. and Vanderbilt D., Theory of polarization: a modern approach, *Physics of Ferroelectrics*, 31 (2007).
[33] Resta R., Posternak M. and Baldereschi A., Towards a quantum theory of polarization in ferroelectrics: The case of $KNbO_3$, *Phys. Rev. Lett.* **70**, 1010 (1993).
[34] Ceperley D. M. and Alder B., Ground state of the electron gas by a stochastic method, *Phys. Rev. Lett.* **45**, 566 (1980).
[35] Dal Corso A., Pseudopotentials periodic table: From H to Pu, *Comput. Mater. Sci.* **95**, 337 (2014).
[36] Momma K. and Izumi F., VESTA 3 for three-dimensional visualization of crystal, volumetric and morphology data, *J. Appl. Crystallogr.* **44**, 1272 (2011).
[37] Soler J. M., Artacho E., Gale J. D., García A., Junquera J., Ordejón P. and Sánchez-Portal D., The SIESTA method for ab initio order-N materials simulation, *J. Phys.: Condens. Matter* **14**, 2745 (2002).
[38] Nosé S., A unified formulation of the constant temperature molecular dynamics methods, *J. Chem. Phys.* **81**, 511 (1984).
[39] Parrinello M. and Rahman A., Polymorphic transitions in single crystals: A new molecular dynamics method, *J. Appl. Phys.* **52**, 7182 (1981).
[40] Hanrahan B., Espinal Y., Neville C., Rudy R., Rivas M., Smith A., Kesim M. and Alpay S., Accounting for the various contributions to pyroelectricity in lead zirconate titanate thin films, *J. Appl. Phys.* **123**, 124104 (2018).
[41] Hanrahan B., Espinal Y., Liu S., Zhang Z., Khaligh A., Smith A. and Alpay S. P., Combining inverse and conventional pyroelectricity in antiferroelectric thin films for energy conversion, *J. Mater. Chem. C* **6**, 9828 (2018).
[42] Huan T. D., Sharma V., Rossetti Jr G. A. and Ramprasad R., Pathways towards ferroelectricity in hafnia, *Phys. Rev. B* **90**, 064111 (2014).
[43] Batra R., Huan T. D., Jones J. L., Rossetti Jr G. and Ramprasad R., Factors favoring ferroelectricity in hafnia: A first-principles computational study, *J. Phys. Chem. C* **121**, 4139 (2017).
[44] Park M. H., Schenk T., Fancher C. M., Grimley E. D., Zhou C., Richter C., LeBeau J. M., Jones J. L., Mikolajick T. and Schroeder U., A comprehensive study on the structural evolution of HfO_2 thin films doped with various dopants, *J. Mater. Chem. C* **5**, 4677 (2017).
[45] Clima S., Wouters D., Adelmann C., Schenk T., Schroeder U., Jurczak M. and Pourtois G., Identification of the ferroelectric switching process and dopant-dependent switching properties in orthorhombic HfO_2: A first principles insight, *Appl. Phys. Lett.* **104**, 092906 (2014).
[46] Sang X., Grimley E. D., Schenk T., Schroeder U. and LeBeau J. M., On the structural origins of ferroelectricity in HfO_2 thin films, *Appl. Phys. Lett.* **106**, 162905 (2015).
[47] Materlik R., Künneth C. and Kersch A., The origin of ferroelectricity in $Hf_{1-x}Zr_xO_2$: A computational investigation and a surface energy model, *J. Appl. Phys.* **117**, 134109 (2015).

[48] Polakowski P. and Müller J., Ferroelectricity in undoped hafnium oxide, *Appl. Phys. Lett.* **106**, 232905 (2015).
[49] Sághi-Szabó G., Cohen R. E. and Krakauer H., First-principles study of piezoelectricity in $PbTiO_3$, *Phys. Rev. Lett.* **80**, 4321 (1998).
[50] Katsouras I., Asadi K., Li M., Van Driel T. B., Kjaer K. S., Zhao D., Lenz T., Gu Y., Blom P. W. and Damjanovic D., The negative piezoelectric effect of the ferroelectric polymer poly (vinylidene fluoride), *Nat. Mater.* **15**, 78 (2016).
[51] Liu S. and Cohen R., Origin of negative longitudinal piezoelectric effect, *Phys. Rev. Lett.* **119**, 207601 (2017).
[52] See Supplemental Materials at [URL] for additional data on rigid-ion primay pyroelectricity of *pure* HfO_2, AIMD simulation with the PBE functional for *pure* HfO_2, the anharmonic potential energy of Si:HfO_2, and the thermal expansion and piezoelectricity of Si:HfO_2.
[53] Perdew J. P., Burke K. and Ernzerhof M., Generalized gradient approximation made simple, *Phys. Rev. Lett.* **77**, 3865 (1996).
[54] Zook J. and Liu S., Pyroelectric effects in thin film, *J. Appl. Phys.* **49**, 4604 (1978).
[55] Tong T., Karthik J., Martin L. W. and Cahill D. G., Secondary effects in wide frequency range measurements of the pyroelectric coefficient of $Ba_{0.6}Sr_{0.4}TiO_3$ and $PbZr_{0.2}Ti_{0.8}O_3$ epitaxial layers, *Phys. Rev. B* **90**, 155423 (2014).
[56] Pandya S., Wilbur J. D., Bhatia B., Damodaran A. R., Monachon C., Dasgupta A., King W. P., Dames C. and Martin L. W., Direct measurement of pyroelectric and electrocaloric effects in thin films, *Phys. Rev. Appl.* **7**, 034025 (2017).
[57] Mart C., Czernohorsky M., Zybell S., Kämpfe T. and Weinreich W., Frequency domain analysis of pyroelectric response in silicon-doped hafnium oxide (HfO_2) thin films, *Appl. Phys. Lett.* **113**, 122901 (2018).
[58] Aigner K., Lengauer W., Rafaja D. and Ettmayer P., Lattice parameters and thermal expansion of Ti(C_xN_{1-x}), Zr(C_xN_{1-x}), Hf(C_xN_{1-x}) and TiN_{1-x} from 298 to 1473 K as investigated by high-temperature X-ray diffraction, *J. Alloys Compd.* **215**, 121 (1994).